nature photonics

LETTERS

https://doi.org/10.1038/s41566-020-0679-9

Check for updates

Optical soliton formation controlled by angle twisting in photonic moiré lattices

Qidong Fu[1,8], Peng Wang[1,8], Changming Huang[2], Yaroslav V. Kartashov[3,4], Lluis Torner[3,5], Vladimir V. Konotop[6,7] and Fangwei Ye[1]✉

Exploration of the impact of synthetic material landscapes featuring tunable geometrical properties on physical processes is a research direction that is currently of great interest because of the outstanding phenomena that are continually being uncovered. Twistronics and the properties of wave excitations in moiré lattices are salient examples. Moiré patterns bridge the gap between aperiodic structures and perfect crystals, thus opening the door to the exploration of effects accompanying the transition from commensurate to incommensurate phases. Moiré patterns have revealed profound effects in graphene-based systems[1–5], they are used to manipulate ultracold atoms[6,7] and to create gauge potentials[8], and are observed in colloidal clusters[9]. Recently, it was shown that photonic moiré lattices enable observation of the two-dimensional localization-to-delocalization transition of light in purely linear systems[10,11]. Here, we employ moiré lattices optically induced in photorefractive nonlinear media[12–14] to elucidate the formation of optical solitons under different geometrical conditions controlled by the twisting angle between the constitutive sublattices. We observe the formation of solitons in lattices that smoothly transition from fully periodic geometries to aperiodic ones, with threshold properties that are a pristine direct manifestation of flat-band physics[11].

By and large, the linear transport and localization properties of excitations in a material are intimately determined by its inner symmetry and geometrical properties, including its periodic or aperiodic nature, in electronic[15], atomic[16,17], optical[18,19] or two-dimensional (2D) material[20] systems. This feature is directly related to the nature of the eigenstates of the system, which can be extended or localized. When an underlying material exhibits a nonlinear response, the formation of self-sustained excitation—that is, solitons—becomes possible[21–23]. Nevertheless, the properties of solitons are still strongly impacted by the linear spectrum of the system. Optical media offer a unique laboratory for the investigation of solitons in different environments. Thus, 2D self-trapping and soliton formation have been investigated in fully periodic optical lattices[13,24–26] as well as in quasicrystals, which are characterized by broken translational invariance[14,27–30]. A common feature of all these results is the occurrence of a power threshold for 2D soliton existence, the value of which can be tuned by varying the lattice configuration[27]; however, the threshold never vanishes. At the same time, formation of solitons at the transition from aperiodic to periodic systems has been never explored experimentally because of a lack of a suitable setting. Optical moiré lattices[11] offer a powerful platform enabling such a study. Created with incommensurate geometries, moiré patterns may enable the localization of light even in the linear limit due to the existence of extremely flat bands in their spectra, a property that strongly impacts the diffraction of beams in such media. Thus, because solitons can emerge due to a balance between diffraction and self-phase modulation induced by nonlinearity, moiré lattices allow investigation of the formation of solitons controlled by the geometry of the induced optical potential. Here, we provide experimental evidence of such a possibility, by reporting qualitative differences in soliton excitation dynamics in commensurate and incommensurate moiré lattices. We present an observation consistent with the formation of thresholdless 2D optical solitons in an aperiodic system, which is enabled by the creation of extremely flat bands in the incommensurate geometry. In addition—and importantly—we demonstrate that in commensurate moiré lattices the threshold for soliton formation is dictated by the area of the primitive lattice cell, which determines the width of the allowed bands. Our observations thus show that the properties of all soliton families are not only determined by the characteristics of the respective gaps, but also fundamentally depend on the properties of the allowed bands.

A photonic moiré lattice can be created in a photorefractive crystal by a shallow modulation of the refractive index in the x–y plane induced by two mutually rotated, or twisted, periodic square sublattices generated by light interference. In our SBN:61 crystal (SBN, strontium barium niobate), where the linear electro-optic effect determines the refractive index modulation experienced by light with different polarizations, the electro-optic coefficient $r_{13}=45\,\mathrm{pm\,V^{-1}}$ is much smaller than $r_{33}=250\,\mathrm{pm\,V^{-1}}$. Accordingly, we used ordinary polarized light for the lattice induction, so that the corresponding beams did not experience any noticeable self-action in the crystal and thus propagated undistorted as in a linear medium. By contrast, light with extraordinary polarization experiences a strong nonlinear response. Propagation along the z direction of a signal beam in such polarization is governed by the nonlinear Schrödinger equation for the dimensionless amplitude $\Psi(\mathbf{r}_\perp,z)$[12,13]:

$$i\frac{\partial\Psi}{\partial z}=-\frac{1}{2}\nabla_\perp^2\Psi+\frac{V_0}{1+I(\mathbf{r}_\perp)+|\Psi|^2}\Psi \qquad (1)$$

Here, $\nabla_\perp=(\partial/\partial x,\partial/\partial y)$, $\mathbf{r}_\perp=(x,y)$ is the radius vector in the transverse plane, z is the longitudinal coordinate scaled to the characteristic

[1]State Key Laboratory of Advanced Optical Communication Systems and Networks, School of Physics and Astronomy, Shanghai Jiao Tong University, Shanghai, China. [2]Department of Electronic Information and Physics, Changzhi University, Shanxi, China. [3]ICFO-Institut de Ciencies Fotoniques, The Barcelona Institute of Science and Technology, Castelldefels, Spain. [4]Institute of Spectroscopy, Russian Academy of Sciences, Troitsk, Moscow, Russia. [5]Universitat Politecnica de Catalunya, Barcelona, Spain. [6]Departamento de Física, Faculdade de Ciências, Universidade de Lisboa, Lisbon, Portugal. [7]Centro de Física Teórica e Computacional, Universidade de Lisboa, Lisbon, Portugal. [8]These authors contributed equally: Qidong Fu, Peng Wang. ✉e-mail: fangweiye@sjtu.edu.cn

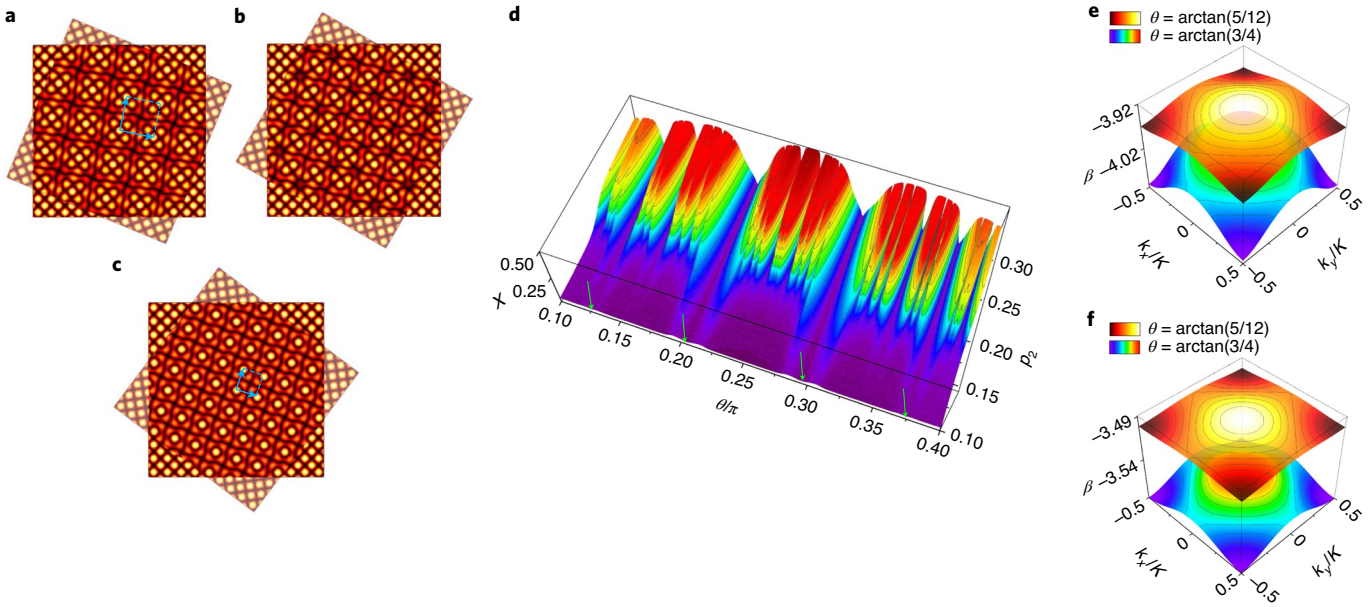

Fig. 1 | Moiré patterns and properties of their linear eigenmodes. a–c, Example of periodic (**a**,**c**) and aperiodic (**b**) moiré lattices $I(\mathbf{r}_\perp)$ produced by two superimposed square sublattices with $p_1 = 0.5$ and $p_2 = 0.3$ rotated by angles $\theta = \arctan(5/12)$ (**a**), $\theta \approx 0.167\pi$ (**b**) and $\theta = \arctan(3/4)$ (**c**). Blue arrows in **a** and **c** indicate the primitive lattice vectors. **d**, Form factor (inverse width) of the most localized linear eigenmode of the lattice versus rotation angle θ and depth p_2 of the second sublattice at $p_1 = 0.5$. Green arrows indicate angles corresponding to the (3,4,5) and (5,12,13) Pythagorean triples. **e**,**f**, The top lattice bands for two Pythagorean angles $\theta = \arctan(3/4)$ and $\theta = \arctan(5/12)$ superimposed in one plot for $p_2 = 0.1$ (**e**) and $p_2 = 0.3$ (**f**). Bloch momenta $k_{x,y}$ are normalized to the width of the Brillouin zone equal to $K \approx 1.265$ for $\theta = \arctan(3/4)$ and to $K \approx 0.785$ for $\theta = \arctan(5/12)$.

length $2\pi n_e \lambda$, where λ is the wavelength (in our experiments $\lambda = 632.8$ nm), n_e is the unperturbed refractive index of the crystal experienced by the extraordinary polarized light and $V_0 > 0$ is the dimensionless applied d.c. field. Here we set $V_0 = 5$, which corresponds to a d.c. electric field of 5.7×10^4 V m^{-1} applied to the crystal, $I(\mathbf{r}_\perp) = \left|p_1 V(\mathbf{r}_\perp) + p_2 V(S\mathbf{r}_\perp)\right|^2$ is the moiré pattern composed of two ordinary polarized periodic sublattices $V(\mathbf{r}_\perp)$ and $V(S\mathbf{r}_\perp)$ interfering in the x–y plane (here $S = S(\theta)$ is the matrix of rotation in the x–y plane by angle θ), and p_1 and p_2 are the amplitudes of the first and second square sublattices, respectively. Each square sublattice $V(\mathbf{r}_\perp)$ is formed by the interference of four plane waves[11]. In the following we set the amplitude of the first sublattice to $p_1 = 0.5$, which corresponds to an average intensity of $I_{av} \approx 1.9$ mW cm^{-2}, and tune the amplitude p_2 of the second sublattice. For such parameters, the actual refractive index modulation depth in the moiré pattern illustrated in Fig. 1a–c is of the order of $\delta n \approx 10^{-4}$.

Two-dimensional Pythagorean moiré lattices composed of two square Bravais sublattices $p_1 V(\mathbf{r}_\perp)$ and $p_2 V(S\mathbf{r}_\perp)$ (the point group D_4), rotated with respect to each other around a common lattice site, are periodic (commensurate) structures only when the rotation angle θ satisfies $\cos\theta = a/c$, $\sin\theta = b/c$, where the positive integers (a, b, c), having no common divisors except 1, constitute a primitive Pythagorean triple, that is, $a^2 + b^2 = c^2$ (Fig. 1a,c). We call such angles Pythagorean. For other rotation angles the pattern is aperiodic (incommensurate, or almost periodic in mathematical terms), as illustrated in Fig. 1b. The linear spectrum of the lattices[10,11] can be obtained by omitting the nonlinear term $|\Psi|^2$ in equation (1) and searching for the corresponding linear eigenmodes in the form $\Psi(\mathbf{r}_\perp, z) = \psi(\mathbf{r}_\perp) e^{i\beta z}$, where β is the linear propagation constant and $\psi(\mathbf{r}_\perp)$ is the transverse field distribution. To characterize the mode localization we use the integral form factor $\chi = \left(\iint |\Psi|^4 \mathrm{d}^2\mathbf{r}_\perp\right)^{1/2} / U$, with U being the mode power $U = \iint |\Psi|^2 \mathrm{d}^2\mathbf{r}_\perp$. Note that the form factor χ is inversely proportional to the mode width, so the larger its value the stronger the mode localization.

The dependence of the form factor of the mode with the largest β (the most localized mode) on θ and p_2 is shown in Fig. 1d. For Pythagorean angles the mode is delocalized for any depth p_2 of the second sublattice, because in this case the moiré pattern is periodic, but for non-Pythagorean angles the mode becomes localized if p_2 exceeds some critical value, $p_2^{cr} \approx 0.18$ corresponding to the linear localization–delocalization threshold. The physical origin of this phenomenon is the suppressed diffraction due to flatness of the allowed bands of the effective Pythagorean lattice approximating a real incommensurate moiré pattern at $p_2 > p_2^{cr}$ (ref. [11]). This observation comes from a general rule: the higher the order of the primitive Pythagorean triple (determined by integer c), the larger the area of the respective primitive cell of the lattice (see the blue arrows in Fig. 1a,c) and the smaller the width (in β) of the allowed bands, thus indicating a reduced diffraction strength. This behaviour is illustrated in Fig. 1e,f, which compares the top bands of the Bloch spectra calculated for two different Pythagorean angles and two different sublattice amplitudes p_2. As discussed in the following, the angular-dependent band flattening has direct implications for soliton formation in the lattices, because it exposes that the diffraction strength experienced by narrow linear inputs in the lattices notably decreases with an increase of the order of the primitive Pythagorean triple. This is particularly clear at $p_2 > p_2^{cr}$, where patterns akin to discrete diffraction are observed in the linear limit, and is less pronounced at $p_2 < p_2^{cr}$, when such patterns coexist with a rapidly expanding broader background.

Turning now to the nonlinear regime, we look for soliton solutions of equation (1) in the form $\Psi(\mathbf{r}_\perp, z) = \psi(\mathbf{r}_\perp) e^{i\beta z}$, where β is the nonlinear propagation constant, which for $V_0 > 0$ (focusing nonlinearity) exceeds the propagation constants of the linear eigenmodes. Solitons form families characterized by the dependencies of the peak amplitude $\psi_{max} = \max|\psi|$ and power U on β, as shown in Fig. 2. Because incommensurate moiré lattices have either delocalized (at $p_2 < p_2^{cr}$) or localized (at $p_2 > p_2^{cr}$) linear modes, solitons

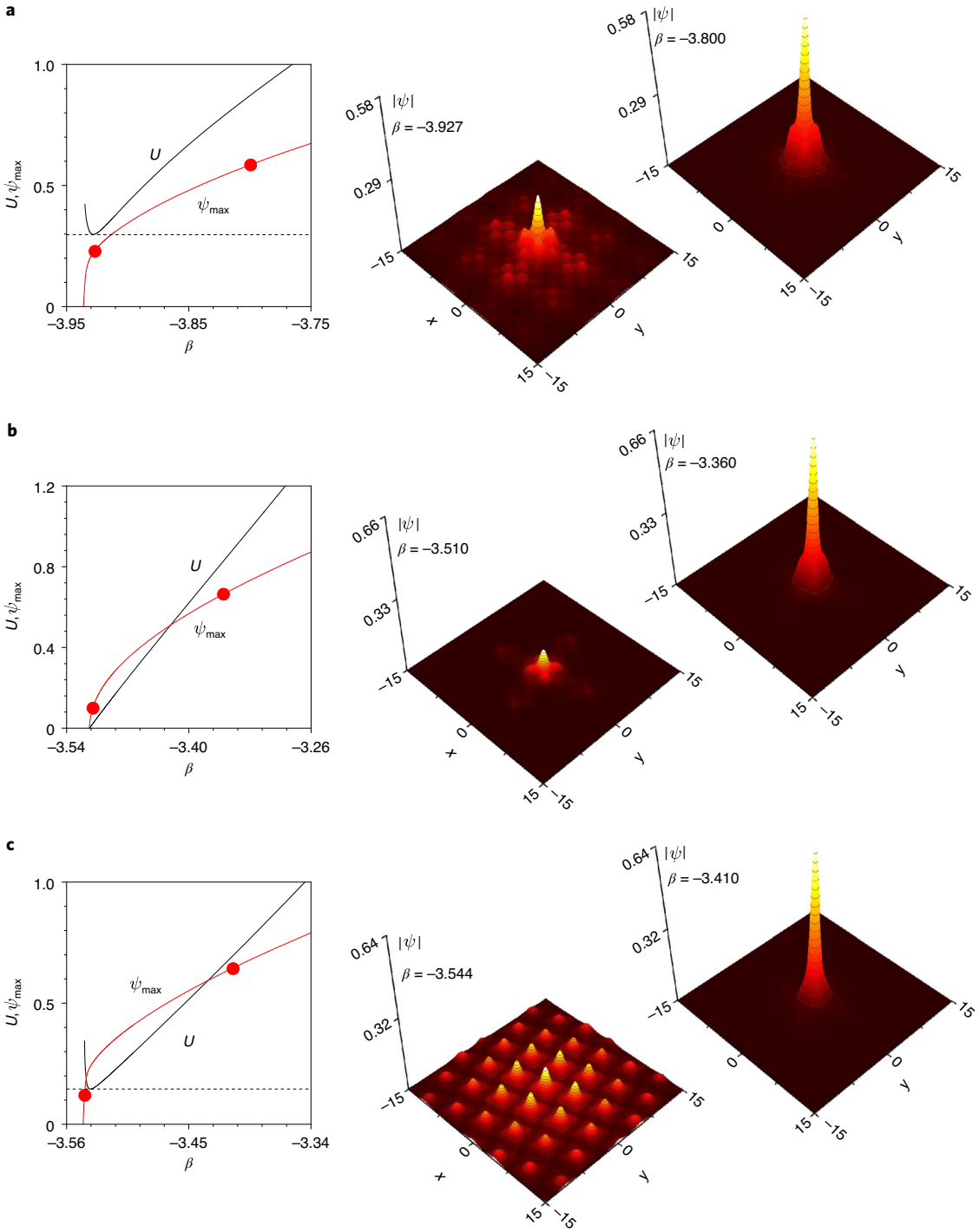

Fig. 2 | Families of 2D solitons in moiré lattices. a–**c**, Soliton power U and peak amplitude ψ_{max} versus propagation constant β (left column) and representative soliton profiles (right column) are shown for a incommensurate moiré lattice with rotation angle $\theta \approx 0.139\pi$ below ($p_2 = 0.1$, **a**) and above ($p_2 = 0.3$, **b**) the critical value p_2^{cr}, as well as for a lattice with the Pythagorean rotation angle $\theta = \arctan(3/4)$ with $p_2 = 0.3$ (**c**). The profiles shown in the right column correspond to the red dots on the $\psi_{max}(\beta)$ curves. The horizontal dashed lines in **a** and **c** indicate the corresponding power thresholds for soliton existence.

in such lattices show a completely different behaviour in the low-amplitude limit depending on the p_2 value. When linear localized modes do not exist ($p_2 < p_2^{cr}$), then, consistent with the behaviour in homogeneous media[31], solitons in incommensurate moiré lattices can exist only if they carry a power U that exceeds a certain threshold value U_{th} (Fig. 2a) below which they quickly diffract. However, when $p_2 > p_2^{cr}$ and linear localized states exist, the soliton family bifurcates from the respective linear localized mode, remaining well-localized at any power U. Under such conditions, solitons do not feature a power existence threshold (Fig. 2b). By contrast, in commensurate moiré lattices corresponding to the Pythagorean angles, solitons always exhibit a non-zero existence

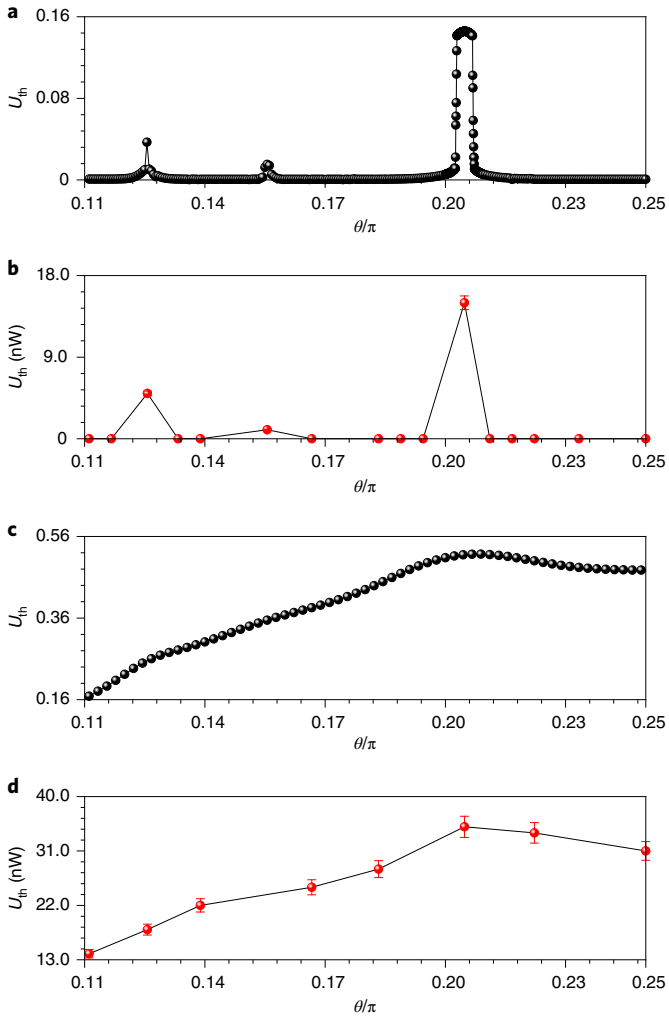

Fig. 3 | Thresholds for soliton formation in moiré lattices. a–d, Comparison of theoretically calculated (**a**,**c**) and experimentally measured (**b**,**d**) dependencies of the threshold for soliton formation on rotation angle θ for the depth of the second sublattice above the localization–delocalization threshold $p_2 = 0.3$ (**a**,**b**) and below the localization–delocalization threshold $p_2 = 0.1$ (**c**,**d**). Error bars in **b** and **d** indicate the systematic uncertainty of the power threshold.

power threshold for any depth of the second sublattice p_2 (Fig. 2c), and strongly expand at low amplitudes. In all the cases shown in Fig. 2, the peak soliton amplitude vanishes in the linear limit (red curves, Fig. 2a–c), while far from it the solitons become strongly localized. All shown soliton families are either completely stable, when the power threshold is zero, or unstable at low amplitudes and become stabilized at high amplitudes, when the power threshold does not vanish.

Here we report the experimental observation of all such scenarios using lattices with readily tunable twisting angle. More specifically, the transition between commensurate and incommensurate moiré lattices or between the regimes where delocalization and localization takes place in the linear limit can be explored by adjusting the phase mask used for the creation of the sublattices or by tuning their relative amplitudes. A comparison between the theoretical predictions and the experimental observations of the threshold power U_{th} as a function of the rotation angle θ between the sublattices is shown in Fig. 3. For p_2 above the critical value (Fig. 3a), U_{th} vanishes for non-Pythagorean angles, but it exhibits narrow peaks around the Pythagorean angles. As is visible in Fig. 1e,f, the band curvature decreases with increasing order of the Pythagorean triple. Thus, the nonlinearity required to balance the curvature-induced diffraction decreases too, in agreement with the observations depicted in Fig. 3a,b. The first, second and third highest peaks occur near the Pythagorean angles corresponding to the primitive triples (3,4,5), (5,12,13) and (8,15,17), respectively. The important conclusion to be highlighted is that the observed power thresholds for soliton formation are directly related to the areas of the respective primitive cells, and thus to the structure of both, the gaps and the allowed bands of the lattice spectrum. The area of the primitive cell of a commensurate Pythagorean lattice, defined by the third integer c, indeed non-monotonically depends on the twist angle, hence the observed non-monotonic variation in the heights of the peaks in Fig. 3a,b, which is in agreement with the variation of primitive cell areas for the corresponding Pythagorean triples. For example, the smallest area of the primitive (square) cell of a Pythagorean moiré pattern corresponds to the primitive triple (3,4,5), which explains the locations of the absolute maxima in all panels of Fig. 3. Because the bands become flatter when the areas of the primitive cells increase, other U_{th} maxima are almost undetectable. This is consistent with the approximation of incommensurate Pythagorean moiré patterns by commensurate ones, as established in ref. [11]. In all experimental results reported, as well as in all numerical simulations showing dynamical soliton excitation, we observed stability of 2D beams.

Remarkably, the above relation between the order of the Pythagorean triple associated with the lattice and the threshold for soliton formation, even though less pronounced, was still observed in the regime $p_2 < p_2^{cr}$, where localization in the linear system is impossible even in incommensurate lattices (Fig. 3c,d). Under these conditions the soliton formation threshold U_{th} does not vanish for any rotation angle, although it remains sensitive to the diffraction properties of the lattice. Our observations show that it achieves a maximal value around an angle of $\theta = \arctan(3/4)$, which corresponds to the commensurate Pythagorean lattice associated with the (3,4,5) triple and having the smallest possible primitive cell. In all cases we observed an excellent agreement between the theoretical predictions (Fig. 3a,c) and the experimental (Fig. 3b,d) results.

The threshold power U_{th} for soliton formation was measured by evaluating the soliton content $C = U_{out}/U_{in}$, where U_{in} is the power of the input beam measured at $z = 0$ and U_{out} is the power of the beam that remains at the output after 2 cm of propagation, within a pinhole of radius of 27 μm approximately equal to one period of the sublattice forming the moiré pattern. In the numerical modelling of the dynamical soliton excitation within the frames of model (1), we used the same criterion calculating the output power for Gaussian inputs $\Psi = A \exp(-\mathbf{r}_\perp^2/r_0^2)$ within a circle of radius equal to the sublattice period, albeit at large propagation distances ($z = 1{,}000$) to avoid the presence of transient effects.

In Fig. 4 we show the dependence of the soliton content C on the input power U, together with the low-power and high-power output beams, for a moiré lattice with $p_2 > p_2^{cr}$ (that is, above the linear localization–delocalization threshold), for different rotation angles. In lattices corresponding to the Pythagorean angles $\arctan(3/4)$ and $\arctan(5/12)$ (black and red lines, Fig. 4a,b), one observes a sharp jump from diffraction to a soliton content close to unity upon an increase of the input power. This means that practically all input power goes into a soliton. The power corresponding to the abrupt increase in C is the dynamical threshold for soliton formation U_{th}—it is this quantity that is plotted in Fig. 3b,d. For non-Pythagorean angles—that is, for incommensurate moiré lattices—soliton content C remains very high, irrespective of the input power (green lines, Fig. 4a,b) because such a lattice supports linear modes that are effectively excited by the input beam. Figure 4c–e illustrates that, for Pythagorean angles, the output beam becomes localized only at sufficiently high power, while for non-Pythagorean angles the

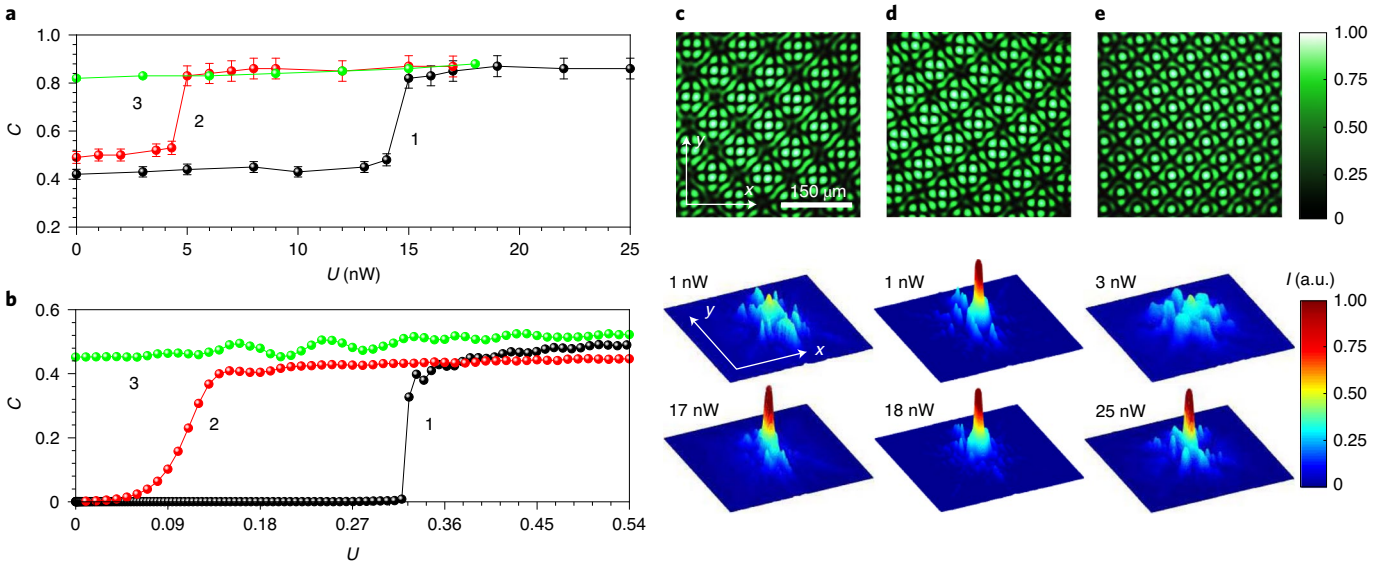

Fig. 4 | Soliton formation above the linear localization–delocalization threshold. a,**b**, Experimentally measured (**a**) and numerical (**b**) soliton content versus input power for Pythagorean rotation angles $\theta = \arctan(3/4)$ (curve 1), $\arctan(5/12)$ (curve 2) and for non-Pythagorean angle 0.139π (curve 3). Error bars in **a** indicate the systematic uncertainty of soliton content. The second sublattice depth is $p_2 = 0.3$. **c**–**e**, Lattice profiles (top row) and observed output signal intensity distribution $I(x,y)$ corresponding to low-power (middle row) and high-power (bottom row) input powers, for $\theta = \arctan(5/12)$ (**c**), $\theta = \arctan(3/4)$ (**e**) and $\theta \approx 0.139\pi$ (**d**) angles. The numbers given in the middle and bottom rows are the input signal powers.

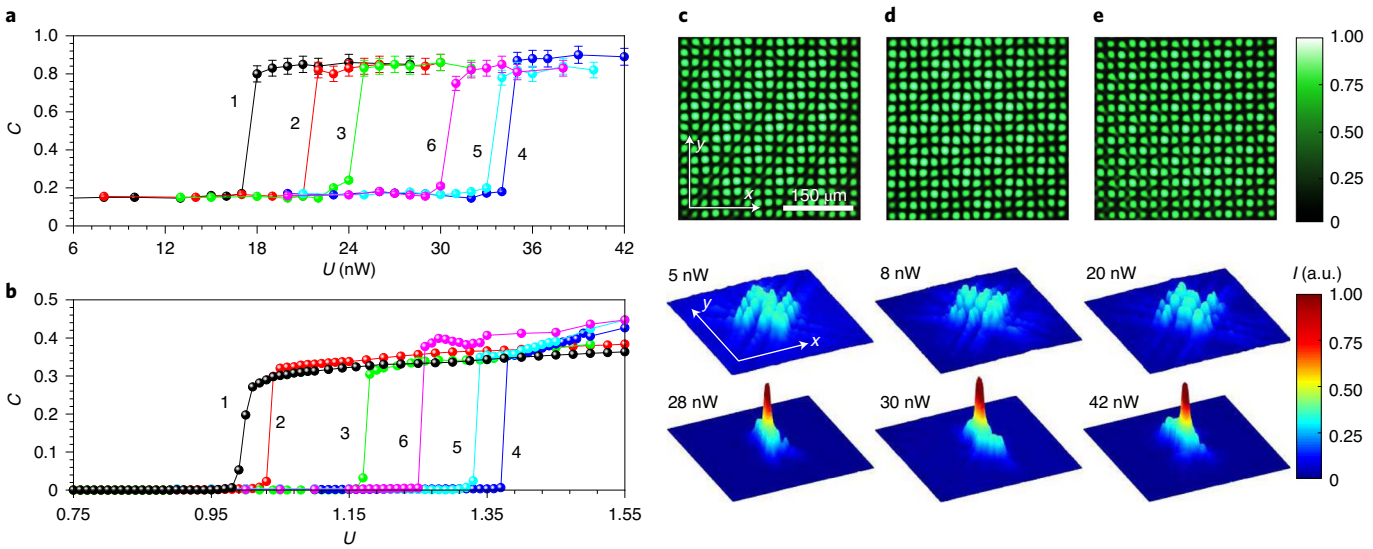

Fig. 5 | Soliton formation below the linear localization–delocalization threshold. a,**b**, Experimentally measured (**a**) and theoretically calculated (**b**) soliton content versus input power for rotation angles $\theta = \arctan(5/12)$ (curve 1), 0.139π (curve 2), 0.167π (curve 3), $\arctan(3/4)$ (curve 4), 0.222π (curve 5) and 0.250π (curve 6) for second sublattice depth $p_2 = 0.1$. Error bars in **a** indicate the systematic uncertainty of soliton content. **c**–**e**, Lattice profiles (top row) and corresponding low-power (middle row) and high-power (bottom row) output light signal intensity distributions $I(x,y)$, for Pythagorean $\theta = \arctan(5/12)$ (**c**), $\theta = \arctan(3/4)$ (**e**) and non-Pythagorean $\theta \approx 0.139\pi$ (**d**) angles. The numbers given in the middle and bottom rows are the input signal powers.

output is always localized, consistent with theoretical predictions and with expectations based on the flatness of the bands at such twisting angles.

The generation of solitons with Gaussian input beams, which differ considerably from the soliton profiles, is not only a further demonstration of their stability but also an indication of the robustness of their excitation process, even when it requires significant beam reshaping. Note that this is in sharp contrast to the case of soliton formation in the finite gaps of moiré lattices: even though the corresponding stationary solutions exhibit existence properties similar to those featured by the stationary soliton families that form in the semi-infinite gap of moiré lattices, all of them are unstable (see Supplementary Information).

Figure 5 depicts the observed behaviour of the soliton content for lattices with $p_2 < p_2^{cr}$, which thus cannot support linear localized states. We observed step-like behaviour of the soliton content

C for all Pythagorean and non-Pythagorean angles. Namely, solitons are excited only above a threshold power (see outputs in Fig. 5a–e). Notice the higher values of the threshold power relative to the previous cases, consistent with Fig. 3c (in all cases the used input powers are well below the saturation limit). Above threshold, the values of *C* are similar for different rotation angles, indicating that the excited states are strongly localized on the scale of about one sublattice period.

Summarizing, we have observed the excitation of 2D solitons in Pythagorean moiré patterns and have shown that their excitation dynamics is dictated by the fundamental transition from commensurate to incommensurate lattice geometries. Incommensurability and the relation between the depths of the two sublattices forming the moiré pattern have been shown to be crucial for soliton excitation. In all cases, the behaviour of the soliton formation threshold is a direct manifestation of the band structure of the moiré lattices resulting from the different twisting angles of the sublattices and, in particular, of the general band flattening associated with the geometry of the moiré lattices. We anticipate that similar phenomena may occur in moiré patterns composed of sublattices of other crystallographic symmetries, such as twisted honeycomb lattices, and in other physical systems where flat bands induced by geometry arise.

Online content

Any methods, additional references, Nature Research reporting summaries, source data, extended data, supplementary information, acknowledgements, peer review information; details of author contributions and competing interests; and statements of data and code availability are available at https://doi.org/10.1038/s41566-020-0679-9.

Received: 12 March 2020; Accepted: 13 July 2020;
Published online: 24 August 2020

References

1. Decker, R. et al. Local electronic properties of graphene on a BN substrate via scanning tunneling microscopy. *Nano Lett.* **11**, 2291–2295 (2011).
2. Woods, C. R. et al. Commensurate–incommensurate transition in graphene on hexagonal boron nitride. *Nat. Phys.* **10**, 451–456 (2014).
3. Cao, Y. et al. Correlated insulator behaviour at half-filling in magic-angle graphene superlattices. *Nature* **556**, 80–84 (2018).
4. Cao, Y. et al. Unconventional superconductivity in magic-angle graphene superlattices. *Nature* **556**, 43–50 (2018).
5. Ahn, S. J. et al. Dirac electrons in a dodecagonal graphene quasicrystal. *Science* **786**, 782–786 (2018).
6. González-Tudela, A. & Cirac, J. I. Cold atoms in twisted-bilayer optical potentials. *Phys. Rev. A* **100**, 053604 (2019).
7. Salamon, T. et al. Simulating twistronics without a twist. *Phys. Rev. Lett.* **125**, 030504 (2020).
8. San-Jose, P., González, J. & Guinea, F. Non-Abelian gauge potentials in graphene bilayers. *Phys. Rev. Lett.* **108**, 216802 (2012).
9. Cao, X., Panizon, E., Vanossi, A., Manini, N. & Bechinger, C. Orientational and directional locking of colloidal clusters driven across periodic surfaces. *Nat. Phys* **15**, 776–780 (2019).
10. Huang, C. et al. Localization–delocalization wavepacket transition in Pythagorean aperiodic potentials. *Sci. Rep.* **6**, 32546 (2016).
11. Wang, P. et al. Localization and delocalization of light in photonic moiré lattices. *Nature* **577**, 42–46 (2020).
12. Efremidis, N. K., Sears, S., Christodoulides, D. N., Fleischer, J. W. & Segev, M. Discrete solitons in photorefractive optically induced photonic lattices. *Phys. Rev. E* **66**, 046602 (2002).
13. Fleischer, J. W., Segev, M., Efremidis, N. K. & Christodoulides, D. N. Observation of two-dimensional discrete solitons in optically induced nonlinear photonic lattices. *Nature* **422**, 147–150 (2003).
14. Freedman, B. et al. Wave and defect dynamics in nonlinear photonic quasicrystals. *Nature* **440**, 1166–1169 (2006).
15. Brandes, T. & Kettemann, S. *The Anderson Transition and its Ramifications*: *Localization*, *Quantum Interference and Interactions* (Springer, 2003).
16. Morsch, O. & Oberthaler, M. Dynamics of Bose–Einstein condensates in optical lattices. *Rev. Mod. Phys.* **78**, 179–215 (2006).
17. Billy, J., Sanchez-Palencia, L., Bouyer, P. & Aspect, A. Direct observation of Anderson localization of matter waves in a controlled disorder. *Nature* **453**, 891–894 (2008).
18. Wiersma, D. S. Disordered photonics. *Nat. Photon.* **7**, 188–196 (2013).
19. Segev, M., Silberberg, Y. & Christodoulides, D. N. Anderson localization of light. *Nat. Photon.* **7**, 197–204 (2013).
20. DasSarma, S., Adam, S., Hwang, E. H. & Rossi, E. Electronic transport in two-dimensional graphene. *Rev. Mod. Phys.* **83**, 407–470 (2011).
21. Lederer, F. et al. Discrete solitons in optics. *Phys. Rep.* **463**, 1–126 (2008).
22. Kartashov, Y. V., Astrakharchik, G., Malomed, B. & Torner, L. Frontiers in multidimensional self-trapping of nonlinear fields and matter. *Nat. Rev. Phys.* **1**, 185–197 (2019).
23. Chen, Z., Segev, M. & Christodoulides, D. N. Optical spatial solitons: historical overview and recent advances. *Rep. Prog. Phys.* **75**, 086401 (2012).
24. Yang, J. & Musslimani, Z. H. Fundamental and vortex solitons in a two-dimensional optical lattice. *Opt. Lett.* **28**, 2094–2096 (2003).
25. Efremidis, N. K. et al. Two-dimensional optical lattice solitons. *Phys. Rev. Lett.* **91**, 213906 (2003).
26. Neshev, D., Ostrovskaya, E., Kivshar, Y. & Krolikowski, W. Spatial solitons in optically induced gratings. *Opt. Lett.* **28**, 710–712 (2003).
27. Ablowitz, M. J., Ilan, B., Schonbrun, E. & Piestun, R. Solitons in two-dimensional lattices possessing defects, dislocations and quasicrystal structures. *Phys. Rev. E* **74**, 035601 (2006) .
28. Law, K. J. H., Saxena, A., Kevrekidis, P. G. & Bishop, A. R. Stable structures with high topological charge in nonlinear photonic quasicrystals. *Phys. Rev. A* **82**, 035802 (2010).
29. Ablowitz, M. J., Antar, N., Bakirtas, I. & Ilan, B. Vortex and dipole solitons in complex two-dimensional nonlinear lattices. *Phys. Rev. A* **86**, 033804 (2012).
30. Xavier, J., Boguslawski, M., Rose, P., Joseph, J. & Denz, C. Reconfigurable optically induced quasicrystallographic three-dimensional complex nonlinear photonic lattice structures. *Adv. Mater.* **22**, 356–360 (2010).
31. Chiao, R. Y., Garmire, E. & Townes, C. H. Self-trapping of optical beams. *Phys. Rev. Lett.* **13**, 479 (1964).

Methods

Experimental set-up. The experiment was carried out in a biased SBN:61 photorefractive crystal with dimensions of $5\times5\times20\,mm^3$. The experimental set-up was similar to the one used in ref. [11]. A continuous-wave laser with wavelength of $\lambda=532\,nm$ and ordinary polarization was used to write the desired moiré lattices into the sample by superposing two square lattice patterns (sublattices) with tunable amplitudes $p_{1,2}$ and twist angles θ. To probe the induced moiré lattice, an extraordinarily polarized beam from a He-Ne laser ($\lambda=632.8\,nm$) was launched into the sample, and its propagation through the sample was monitored. The power of the probe beam could be varied in the range from several nanowatts to microwatts by using a variable attenuator to control the nonlinear self-action due to photorefractive nonlinearity. The beam power in preset pinholes with desired radius R, connected to the soliton content, was acquired using a laser beam profiler.

Data availability

The data that support the plots within this paper and other findings of this study are available from the corresponding author.

Code availability

The codes that support the findings of this study are available from the corresponding author upon reasonable request.

Acknowledgements

Q.F., P.W. and F.Y. acknowledge support from NSFC (grants 91950120 and 11690033) and the Natural Science Foundation of Shanghai (grant 19ZR1424400). P.W. and F.Y. thank X. Chen for support with experiments. Y.V.K. and L.T. acknowledge support from the Severo Ochoa Excellence Programme, Fundacio Privada Cellex, Fundacio Privada Mir-Puig and CERCA/Generalitat de Catalunya. V.V.K. acknowledges financial support from the Portuguese Foundation for Science and Technology (FCT) under contract no. UIDB/00618/2020.

Author contributions

All authors contributed significantly to the work.

Competing interests

The authors declare no competing interests.

Additional information

Supplementary information is available for this paper at https://doi.org/10.1038/s41566-020-0679-9.

Correspondence and requests for materials should be addressed to F.Y.

Reprints and permissions information is available at www.nature.com/reprints.